Quasimonoenergetic multi-GeV electron acceleration in a plasma waveguide

Ronan Lahaye,[1] Kosta Oubrerie,[2] Olena Kononenko,[1] Julien Gautier,[1] Igor A. Andriyash,[1] and Cedric Thaury[1,*]

[1]*Laboratoire d'Optique Appliquée, ENSTA, CNRS, Ecole Polytechnique, Institut Polytechnique de Paris, 828 Bd des Maréchaux, 91762 Palaiseau, France*

[2]*Université Paris-Saclay, CEA, LIDYL, 91191 Gif-sur-Yvette, France*

(Received 1 April 2025; accepted 6 August 2025; published 11 September 2025)

Laser-plasma accelerators present a promising alternative to conventional accelerators. To fully exploit the extreme amplitudes of the plasma fields and produce high-quality beams, precise control over electron injection into the accelerating structure is required, along with effective laser pulse guiding to extend the acceleration length. Recent studies have demonstrated efficient guiding and acceleration using hydrodynamic optically field-ionized plasma channels. This guiding technique has also been combined with controlled electron injection to produce high-quality electron beams at the GeV level using a 50 TW laser. The present work extends these results to higher laser power, demonstrating the generation of quasimonoenergetic electron beams with peak energies exceeding 2 GeV, for a PW-class laser.

DOI: 10.1103/39x8-jgvw

I. INTRODUCTION

Laser-wakefield acceleration relies on the use of an ultrashort and ultraintense ($I \gtrsim 10^{18}$ W cm^{-2}) laser pulse, ionizing a light gas, and creating an underdense plasma. Propagating through the plasma, the laser pulse drives an accelerating structure for the electrons in its wake [1]. To maintain this accelerating structure over long distances, it is necessary to keep the laser pulse focused along the propagation in the plasma. One way to achieve this is to create a long plasma filament beforehand and let it expand radially to obtain a curved radial density profile with a minimum electron density on the laser axis. This density profile corresponds to a curved refractive index profile, with a maximum at the center, acting then as graded-index optical fiber, keeping the driver pulse focused along the propagation. Several energy records in laser-plasma acceleration were established using plasma waveguides created with capillary discharges [2,3]. However, this method makes it difficult to tailor the longitudinal density profile and is especially prone to material damage.

These difficulties have led to the development of an alternate guiding scheme, using a secondary laser pulse focused in a line by an axicon [4–6] or an axiparabola [7,8], creating a quasi-Bessel beam with a long focal line over which the laser spot size varies slowly. This secondary laser pulse generates, through optical-field ionization (OFI), the plasma filament which ultimately results in the formation of the waveguide. This technique was first demonstrated using density transition injection [9] with 100 TW-class lasers, allowing the reliable production of high-quality electron beams at the GeV energy level [10]. The first attempt with a PW laser, without controlled injection produced beams of up to 5 GeV, but with a large shot-to-shot variation and a significant component at low energies [11,12]. Later, in another study, a 100 TW-class laser was used to generate high-quality GeV electron beams, confirming the robustness of controlled injection at this power level [13]. Finally, the implementation of controlled injection with a PW laser enabled the generation of high-quality multi-GeV beams [14] up to 10 GeV [15].

Here, we build upon these works by comparing three experimental conditions. Ionization injection with self-guiding, shock-assisted ionization injection [16] with self-guiding, and shock-assisted ionization injection with a plasma waveguide, to produce multi-GeV electron beams with peaked energy spectra.

II. EXPERIMENTAL SETUP

The experiment was carried out at the Apollon laser facility in the long focal area, using the F2 beam which delivers up to 12 J, in a 30 fs laser pulse at a central wavelength of $\lambda_0 = 800$ nm, at a repetition rate of 1 pulse per minute. During the experiment, the laser pulse was chirped to ~60 fs, operating at 12 J. A simplified setup of the experiment is displayed in Fig. 1. The drive laser is focused by a 6-m focal-length spherical mirror to a 45 μm full-width-at-half-maximum (FWHM) focal spot, as shown

*Contact author: cedric.thaury@ensta-paris.fr

Published by the American Physical Society under the terms of the Creative Commons Attribution 4.0 International license. Further distribution of this work must maintain attribution to the author(s) and the published article's title, journal citation, and DOI.

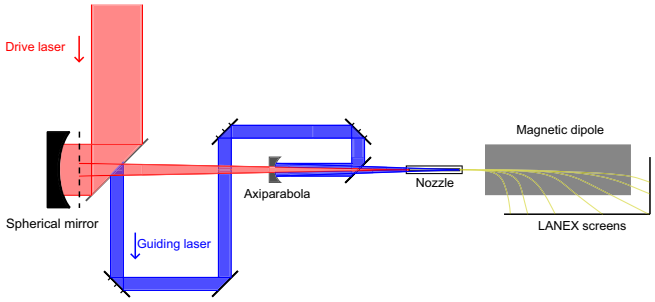


FIG. 1. Simplified setup of the experiment. The guiding laser is represented in blue, and the drive laser in red. The electron energy is measured by a spectrometer consisting of a dipole magnet and two LANEX scintillating screens. The long focal distance of the spherical mirror is not shown and is represented by the vertical dotted line for simplicity.

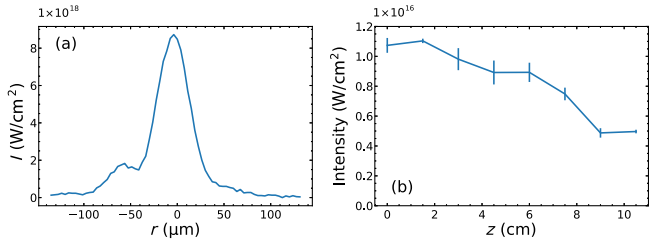


FIG. 2. Focal spot of the drive laser and evolution of the intensity along the focal line of the guiding laser. (a) Measured focal spot of the drive laser. (b) Evolution of the intensity on axis of the guiding laser, the error bars represent the statistical variation over five shots.

in Fig. 2(a), resulting in a normalized potential vector $a_0 \approx 2$. The energy encircled in the first dark ring was estimated to be ≈37%. The guiding laser is generated by a portion of the drive laser extracted through a holed mirror before the spherical mirror which focuses the drive laser. It is attenuated down to ≈40 mJ, then focused by a holed axiparabola with a nominal focal length $f_0 = 600$ mm and maximum focal depth $\delta_0 = 150$ mm, to create a focal line about 8 cm long which generates a plasma filament in the gas target. The focal line of the axiparabola is defined by $f(r) = f_0 + 1/a \ln(r/R \times e^{a\delta_0})$, with $a = 1/\delta_0 \ln(R/r_{\text{hole}})$, and where $r, r_{\text{hole}} = 7.5$ mm, $R = 25.4$ mm are the radial coordinate, the radius of the hole, and the radius of the axiparabola. The focal spot diameter at first zero decreases from 36 μm at the beginning of the focal line to 34.7 μm at the end of the line. The evolution of the on-axis intensity of the guiding laser is shown in Fig. 2(b). The filament then expands for 6 ns before the drive laser is focused in the waveguide and generates the wakefield. The delay between the guiding laser and the drive laser is adjusted through various delay lines in the chamber not represented in Fig. 1.

The target is a 6 cm long slit nozzle supplied with a mixture of 1% nitrogen and 99% helium gas at a backing pressure of 60 bar. To estimate the electronic density reached during the experiment, we measured the longitudinal phase shift experienced by a low-power laser beam as it propagates in the gas flow. To ensure a sufficiently high measured phase shift, the measurement was performed using nitrogen. Using this technique, we measure an average particle density of $n \sim 5 \times 10^{17}$ cm^{-3}, 2 mm above the nozzle, at an operating pressure of 60 bar. Assuming full ionization of the helium gas used in the experiment, this corresponds to an electronic density of $n_e \sim 1 \times 10^{18}$ cm^{-3}. A small blade can be placed at the entrance of the nozzle to tailor the longitudinal density profile and trigger shock-assisted ionization injection, typically producing low-charge and low-dispersion electron beams [16]. A 120 cm, 1.3 T permanent magnetic dipole deflects the electron beam which then impacts on scintillating LANEX regular screens. The screens are imaged onto several 8-bit CMOS cameras, and the resulting signal is analyzed to reconstruct the energy spectrum of the electron beam. The beam charge is estimated by comparing the signal collected on the cameras to the signal emitted by tritium capsules, whose activity and equivalent charge is known [17]. A 180 μm thick magnesium membrane isolates the dipole vacuum chamber from the main experimental chamber. The crossing of this membrane slightly increases the electron beam divergence. In a separate experimental campaign, under similar conditions, the bremsstrahlung radiation produced by the crossing of the membrane was recorded, allowing to measure the entrance angle of the electron beam into the magnet for each shot. During our experiment, we did not have this diagnostic, so we used this data to compute three different dispersion relations, corresponding to an angle of the electron beam and the magnet axis of $\theta_e = 2.9 \pm 6.9$ mrad, where a positive angle corresponds to the counterclockwise direction, and the uncertainty corresponds to the standard deviation of the distribution. The dispersion relations obtained for the high-energy

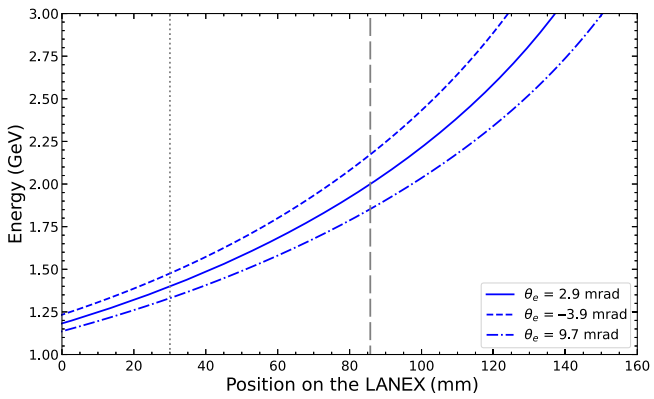


FIG. 3. Dispersion relation of the high-energy LANEX screen. Three dispersion relations are shown for three different entrance angles in the dipole. The dotted and dashed vertical lines correspond to the positions of an electron beam at 1.4 and 2 GeV, respectively, for $\theta_e = 2.9$ mrad.

LANEX are shown in Fig. 3. Considering an electron beam at 2 GeV for an angle of 2.9 mrad, the uncertainty due to the variation of the angle of the electron is about 160 MeV, while it is about 72 MeV for an electron beam at 1.4 GeV for the same angle.

III. RESULTS

With a backing pressure of 60 bar and without the guiding laser and without the blade to trigger the injection, we obtained continuous spectra like those displayed in Fig. 4. The broad spectra are typical of ionization injection, where electron trapping occurs once the normalized potential vector $a_0 \gtrsim 1.8$, a condition generally sustained over long distances in a laser-plasma accelerator [18,19]. The electron beam also demonstrates good shot-to-shot stability, as illustrated by consecutive shots (b) and (c). This characteristic is inherent in the longitudinal nature of the injection technique [20,21]. Although the beam shows little variation from shot to shot, the day-to-day fluctuations in laser properties can lead to more significant changes, with, for instance, the maximum energy varying from 1.25 to 1.4 GeV from day to day, as illustrated in Fig. 4. Significant vignetting in our imaging system prevented reconstruction of the electron spectrum in the 1.05 to 1.18 GeV range. Therefore, to estimate the total charge above 750 MeV, we interpolated the signal within this range, resulting in a charge of approximately 100 pC on day 1 [Fig. 4(a)] and 30 pC on day 2 [Figs. 4(b) and 4(c)]. The maximum charge density above 1.2 GeV is about 0.1 pC/MeV for all shots.

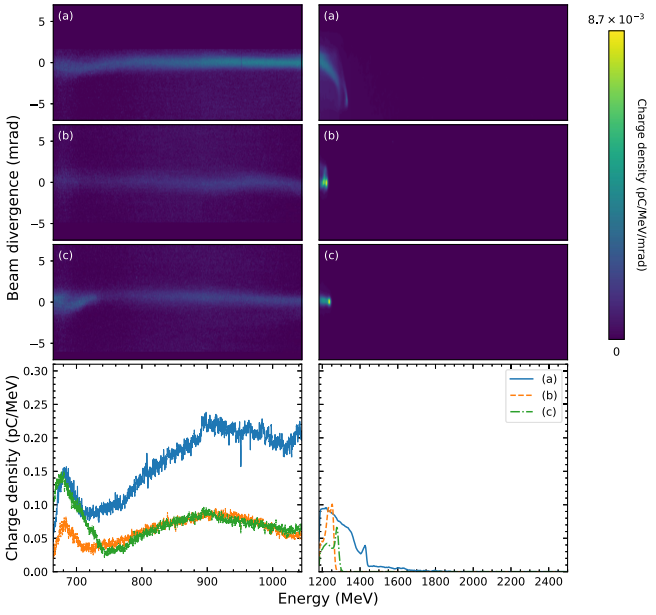


FIG. 4. Top: angularly resolved electron spectra obtained without guiding and with ionization injection. Shots in (b) and (c) are consecutive shots, while (a) was obtained on a different day. Bottom: same spectra but angularly integrated.

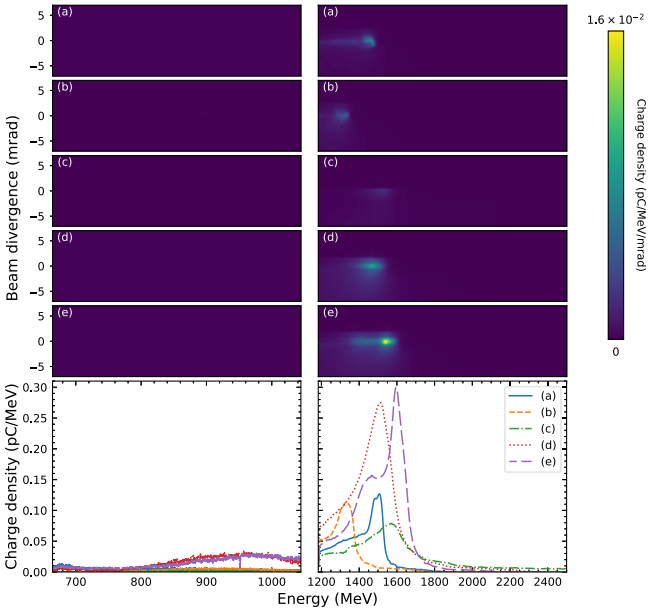


FIG. 5. Top: angularly resolved spectra obtained without guiding and with shock-assisted ionization injection. Bottom: same spectra but angularly integrated.

To increase this value and achieve a peaked energy spectrum, it is necessary to localize the injection. We achieved this level of control using the shock-assisted ionization injection technique. The highest energies were achieved for a backing pressure of 50 bar, as illustrated by the five consecutive spectra shown in Fig. 5. We observe high-energy peaked spectra with almost no charge below 1.1 GeV, a notably increased charge density at high energies, and a maximum energy approximately 16% higher than without shock, exceeding 1.6 GeV for the best shots. The beam charge varies between 20.5 and 83 pC, while the relative energy spread ranges from 6.1% to 20% FWHM. This shot-to-shot variation of the beam features is probably due to the poor stability of the laser focal spot. Despite this, shock-assisted ionization injection provides remarkable beam quality and stability for a PW-class laser system.

We also observe in Fig. 5 that the spectra are strongly asymmetric, with a sharp drop in charge density at high energies and a slower decay toward low energies. Quantitatively, this translates into a peak-to-average energy ratio of the order of 1.1 for shots (a) and (e), which would be 1 for a symmetric beam. This suggests that the acceleration length is close to the dephasing length L_d. Indeed, in the bubble regime, the electrons experience a longitudinal accelerating field proportional to their position within the plasma cavity, ranging from maximum acceleration at the back of the bubble to the decelerating fields at the front. This results in a accumulation of electrons at the maximum energy as the beam reaches the center of the cavity, where the field turns negative [22]. This

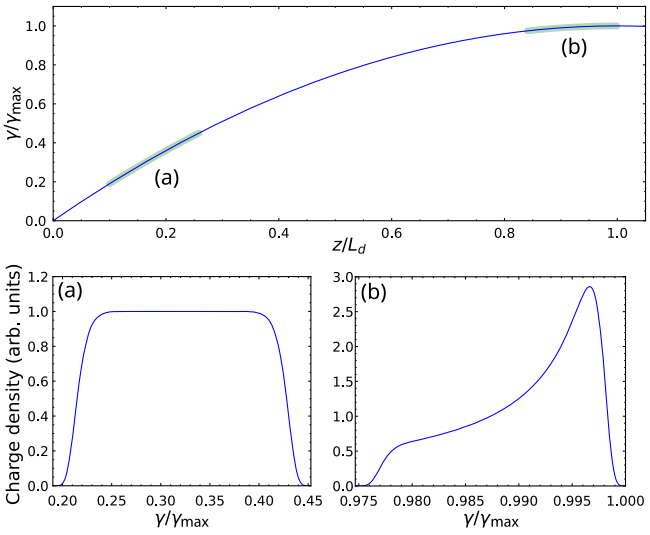


FIG. 6. Electron dephasing in the bubble regime. Top panel: electrons injected at the back of the plasma cavity are accelerated to the dephasing length L_d and then lose energy. The beam chirp is reduced when the beam reaches the vertex of $\gamma(z)$. Panel (a) shows the initial beam energy spread, panel (b) shows the steepening and decrease of the energy spread at the dephasing peak.

phenomenon is illustrated in Fig. 6, which depicts the ideal case of a finite-length beam injected into a linear field propagating at a speed slower than the electron bunch. As shown in panels (a) and (b) of Fig. 6, while the beam's length remains constant, the energy spectrum's width is significantly compressed when it reaches the center of the cavity ($z = L_d$), with a bunching at the peak energy. With this simple model explaining how dephasing can modify the energy spread, we can infer that the asymmetric shape of the spectra is an indication that the plasma density is optimal, with the dephasing length closely matching the laser's effective propagation length. A lower plasma density would reduce the accelerating field, while a higher density would enhance dephasing, leading to reduced energy in both cases.

We can use Lu's model to evaluate the effective acceleration length, identifying it with the dephasing length. According to this model, the maximum energy gain ΔW is linked to the electronic density n_e through [23]

$$\frac{\Delta W}{m_e c^2} = \frac{2}{3}\frac{n_c}{n_e} a_0, \tag{1}$$

leading, in our case, for $a_0 \approx 2$, and considering $\Delta W \approx 1.7$ GeV, to a density of $n_e \approx 7 \times 10^{17}$ cm^{-3}, which is close to the measured average density, after accounting for the change in operating pressure between the measurement and the shooting conditions. The dephasing length is then

$$L_d = \frac{1}{k_p}\frac{4}{3}\frac{n_c}{n_e}\sqrt{a_0}, \tag{2}$$

which leads to $L_d \approx 3$ cm. For this density and this pulse duration, we also evaluate the etching length to be on the order of $L_{\text{etch}} \approx 4.5$ cm, which is consistent with an acceleration being limited by dephasing. This simple model suggests that only about half of the target is used for acceleration and points out the need to guide the beam to reach higher energies.

The implementation of an OFI waveguide allowed us to achieve this guiding. As the formation of the waveguide significantly reduces the on-axis density, we had to increase the backing pressure to keep the density high enough for injection. With a backing pressure of 70 bar, the maximum available, we obtained the spectra displayed in Fig. 7. These spectra were recorded immediately after those shown in Fig. 5, under the same laser conditions. Due to the pointing instability of the drive laser, the coupling efficiency into the waveguide fluctuated significantly from shot to shot, resulting in many shots with little or no charge injection [10]. Figure 7, therefore, displays only the two best shots from a series of 18 shots. Despite being selected spectra, it is worth noting that the maximum energy achieved in these shots significantly surpasses that measured in all shots without guiding. The spectra show relative energy spreads (9% and 12%, respectively) and beam charges (21 and 47 pC) comparable to those measured without the waveguide, while achieving significantly higher energies (1.9 and 2 GeV). Since we never observed electron energies that high when shooting without the guiding laser, we attribute this increase in energy gain by 400–500 MeV, without any loss in charge or beam quality, to the successful increase of the acceleration length through the guiding of the drive laser in the waveguide.

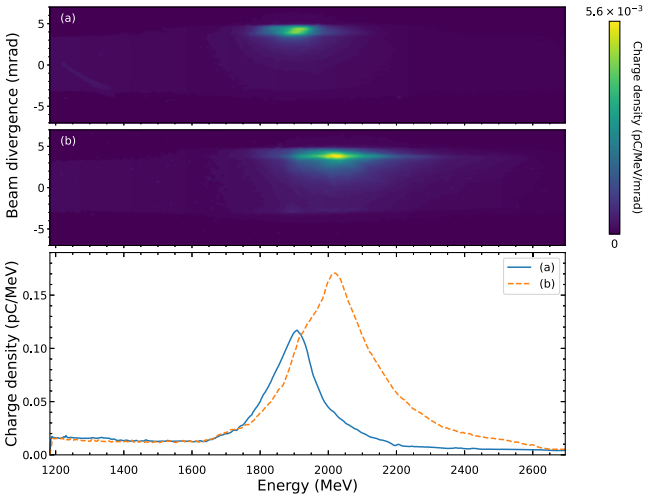


FIG. 7. Top: angularly resolved spectra obtained with guiding and shock-assisted ionization injection. Bottom: same spectra but angularly integrated.

IV. DISCUSSION

To assess the performance of the accelerator, we have to estimate the density in the plasma waveguide. From previous studies [24], we can estimate that the channel-forming beam reduces the on-axis density by a factor of 4 to 6. Taking into account the increase in operating pressure between the nonguided case and the guided case (from 50 to 70 bar) leads to a density in the plasma waveguide between 2 and 3×10^{17} cm^{-3}. Using Lu's model and assuming a parabolic evolution of the energy gain due to dephasing, we can estimate roughly the optimal acceleration length and maximum energy gain for these densities. For a deep channel, the maximum energy gain is around 6 GeV over 20 cm of acceleration, and a shallow channel leads to around 4 GeV of energy gain over 10 cm. Considering smaller acceleration lengths, closer to the length of our target, we estimate the energy gain over 6 cm of acceleration with a constant density profile to be around 3 GeV, which is slightly higher than the cutoff energy measured with the guiding beam (Fig. 7). This discrepancy could be attributed to potential inhomogeneities in the target density profile, particularly a descending density gradient at the end of the propagation. Such a gradient reduces the amplitude of the accelerating electric field and increases the dephasing rate.

In summary, we demonstrated the production of a multi-GeV electron beam with a peaked energy spectrum using a hydrodynamic shock for injection and an OFI waveguide to guide the laser through a 6 cm-long plasma. The results suggest that the electron energy is primarily limited by the target length. With the same plasma density and laser energy as in Fig. 7, extending the target to tens of centimeters could enable energy gains exceeding 5 GeV, similar to those achieved at other PW-laser facilities [6,11]. To further optimize the setup, the implementation of an active pointing stabilization system [25] could ensure a precise overlap of the guiding and drive lasers, improving laser coupling into the waveguide on every shot. This would enhance both the stability and quality of the electron beam, leading to a reliable multi-GeV source suitable for demanding applications such as free-electron lasers [26,27] or the probing of quantum electrodynamic processes [28].

ACKNOWLEDGMENTS

The authors acknowledge the national research infrastructure Apollon and the LULI for their technical assistance. The project has received funding from the European Union's Horizon 2020 Research and Innovation programme under the Grant Agreement No. 871124, Innovation Fostering in Accelerator Science and Technology (I.FAST), and from the French Agence Nationale de la Recherche (ANR) under Project No. ANR-19-TERC-0001-01.

DATA AVAILABILITY

The data that support the findings of this article are not publicly available upon publication because it is not technically feasible and/or the cost of preparing, depositing, and hosting the data would be prohibitive within the terms of this research project. The data are available from the authors upon reasonable request.

[1] T. Tajima and J. M. Dawson, Laser electron accelerator, Phys. Rev. Lett. **43**, 267 (1979).

[2] W. P. Leemans, B. Nagler, A. J. Gonsalves, C. Tóth, K. Nakamura, C. G. R. Geddes, E. Esarey, C. B. Schroeder, and S. M. Hooker, GeV electron beams from a centimetre-scale accelerator, Nat. Phys. **2**, 696 (2006).

[3] A. J. Gonsalves *et al.*, Petawatt laser guiding and electron beam acceleration to 8 GeV in a laser-heated capillary discharge waveguide, Phys. Rev. Lett. **122**, 084801 (2019).

[4] R. J. Shalloo, C. Arran, A. Picksley, A. von Boetticher, L. Corner, J. Holloway, G. Hine, J. Jonnerby, H. M. Milchberg, C. Thornton, R. Walczak, and S. M. Hooker, Low-density hydrodynamic optical-field-ionized plasma channels generated with an axicon lens, Phys. Rev. Accel. Beams **22**, 041302 (2019).

[5] A. Picksley, A. Alejo, R. J. Shalloo, C. Arran, A. von Boetticher, L. Corner, J. A. Holloway, J. Jonnerby, O. Jakobsson, C. Thornton, R. Walczak, and S. M. Hooker, Meter-scale conditioned hydrodynamic optical-field-ionized plasma channels, Phys. Rev. E **102**, 053201 (2020).

[6] B. Miao, L. Feder, J. E. Shrock, A. Goffin, and H. M. Milchberg, Optical guiding in meter-scale plasma waveguides, Phys. Rev. Lett. **125**, 074801 (2020).

[7] S. Smartsev, C. Caizergues, K. Oubrerie, J. Gautier, J.-P. Goddet, A. Tafzi, K. T. Phuoc, V. Malka, and C. Thaury, Axiparabola: A long-focal-depth, high-resolution mirror for broadband high-intensity lasers, Opt. Lett. **44**, 3414 (2019).

[8] K. Oubrerie, I. A. Andriyash, R. Lahaye, S. Smartsev, V. Malka, and C. Thaury, Axiparabola: A new tool for high-intensity optics, J. Opt. **24**, 045503 (2022).

[9] H. Suk, N. Barov, J. B. Rosenzweig, and E. Esarey, Plasma electron trapping and acceleration in a plasma wake field using a density transition, Phys. Rev. Lett. **86**, 1011 (2001).

[10] K. Oubrerie, A. Leblanc, O. Kononenko, R. Lahaye, I. A. Andriyash, J. Gautier, J.-P. Goddet, L. Martelli, A. Tafzi, K. Ta Phuoc, S. Smartsev, and C. Thaury, Controlled acceleration of GeV electron beams in an all-optical plasma waveguide, Light Sci. Appl. **11**, 180 (2022).

[11] J. E. Shrock, B. Miao, L. Feder, and H. M. Milchberg, Meter-scale plasma waveguides for multi-GeV laser wakefield acceleration, Phys. Plasmas **29**, 073101 (2022).

[12] B. Miao, J. E. Shrock, L. Feder, R. C. Hollinger, J. Morrison, R. Nedbailo, A. Picksley, H. Song, S. Wang, J. J. Rocca, and H. M. Milchberg, Multi-GeV electron bunches from an all-optical laser wakefield accelerator, Phys. Rev. X **12**, 031038 (2022).

[13] A. Picksley, J. Chappell, E. Archer, N. Bourgeois, J. Cowley, D. R. Emerson, L. Feder, X. J. Gu, O. Jakobsson, A. J. Ross,

W. Wang, R. Walczak, and S. M. Hooker, All-optical GeV electron bunch generation in a laser-plasma accelerator via truncated-channel injection, Phys. Rev. Lett. **131**, 245001 (2023).

[14] J. E. Shrock, E. Rockafellow, B. Miao, M. Le, R. C. Hollinger, S. Wang, A. J. Gonsalves, A. Picksley, J. J. Rocca, and H. M. Milchberg, Guided mode evolution and ionization injection in meter-scale multi-GeV laser wakefield accelerators, Phys. Rev. Lett. **133**, 045002 (2024).

[15] A. Picksley, J. Stackhouse, C. Benedetti, K. Nakamura, H. E. Tsai, R. Li, B. Miao, J. E. Shrock, E. Rockafellow, H. M. Milchberg, C. B. Schroeder, J. van Tilborg, E. Esarey, C. G. R. Geddes, and A. J. Gonsalves, Matched guiding and controlled injection in dark-current-free, 10-GeV-class, channel-guided laser-plasma accelerators, Phys. Rev. Lett. **133**, 255001 (2024).

[16] C. Thaury, E. Guillaume, A. Lifschitz, K. Ta Phuoc, M. Hansson, G. Grittani, J. Gautier, J. P. Goddet, A. Tafzi, O. Lundh, and V. Malka, Shock assisted ionization injection in laser-plasma accelerators, Sci. Rep. **5**, 16310 (2015).

[17] T. Kurz, J. P. Couperus, J. M. Krämer, H. Ding, S. Kuschel, A. Köhler, O. Zarini, D. Hollatz, D. Schinkel, R. D'Arcy, J.-P. Schwinkendorf, J. Osterhoff, A. Irman, U. Schramm, and S. Karsch, Calibration and cross-laboratory implementation of scintillating screens for electron bunch charge determination, Rev. Sci. Instrum. **89**, 093303 (2018).

[18] M. Chen, Z.-M. Sheng, Y.-Y. Ma, and J. Zhang, Electron injection and trapping in a laser wakefield by field ionization to high-charge states of gases, J. Appl. Phys. **99**, 056109 (2006).

[19] A. Pak, K. A. Marsh, S. F. Martins, W. Lu, W. B. Mori, and C. Joshi, Injection and trapping of tunnel-ionized electrons into laser-produced wakes, Phys. Rev. Lett. **104**, 025003 (2010).

[20] S. Corde, C. Thaury, A. Lifschitz, G. Lambert, K. Ta Phuoc, X. Davoine, R. Lehe, D. Douillet, A. Rousse, and V. Malka, Observation of longitudinal and transverse self-injections in laser-plasma accelerators, Nat. Commun. **4**, 1501 (2013).

[21] A. Döpp, B. Mahieu, A. Lifschitz, C. Thaury, A. Doche, E. Guillaume, G. Grittani, O. Lundh, M. Hansson, J. Gautier, M. Kozlova, J. P. Goddet, P. Rousseau, A. Tafzi, V. Malka, A. Rousse, S. Corde, and K. Ta Phuoc, Stable femtosecond x-rays with tunable polarization from a laser-driven accelerator, Light Sci. Appl. **6**, e17086 (2017).

[22] A. Döpp, C. Thaury, E. Guillaume, F. Massimo, A. Lifschitz, I. Andriyash, J.-P. Goddet, A. Tazfi, K. Ta Phuoc, and V. Malka, Energy-chirp compensation in a laser wakefield accelerator, Phys. Rev. Lett. **121**, 074802 (2018).

[23] W. Lu, M. Tzoufras, C. Joshi, F. S. Tsung, W. B. Mori, J. Vieira, R. A. Fonseca, and L. O. Silva, Generating multi-GeV electron bunches using single stage laser wakefield acceleration in a 3D nonlinear regime, Phys. Rev. ST Accel. Beams **10**, 061301 (2007).

[24] R. J. Shalloo, C. Arran, L. Corner, J. Holloway, J. Jonnerby, R. Walczak, H. M. Milchberg, and S. M. Hooker, Hydrodynamic optical-field-ionized plasma channels, Phys. Rev. E **97**, 053203 (2018).

[25] G. Genoud, F. Wojda, M. Burza, A. Persson, and C.-G. Wahlström, Active control of the pointing of a multi-terawatt laser, Rev. Sci. Instrum. **82**, 033102 (2011).

[26] W. Wang, K. Feng, L. Ke, C. Yu, Y. Xu, R. Qi, Y. Chen, Z. Qin, Z. Zhang, M. Fang, J. Liu, K. Jiang, H. Wang, C. Wang, X. Yang, F. Wu, Y. Leng, J. Liu, R. Li, and Z. Xu, Free-electron lasing at 27 nanometres based on a laser wakefield accelerator, Nature (London) **595**, 516 (2021).

[27] M. Labat *et al.*, Seeded free-electron laser driven by a compact laser plasma accelerator, Nat. Photonics **17**, 150 (2023).

[28] A. Di Piazza, C. Müller, K. Z. Hatsagortsyan, and C. H. Keitel, Extremely high-intensity laser interactions with fundamental quantum systems, Rev. Mod. Phys. **84**, 1177 (2012).